Accurate Concentration Recovery for Quantitative Magnetic Particle Imaging Reconstruction via Nonconvex Regularization

Tao Zhu, Lin Yin, Jie He, Zechen Wei, Xin Yang, Jie Tian, *Fellow, IEEE,*
and Hui Hui, *Member, IEEE*

Abstract—**Magnetic particle imaging (MPI) uses nonlinear response signals to noninvasively detect magnetic nanoparticles in space, and its quantitative properties hold promise for future precise quantitative treatments. In reconstruction, the system matrix based method necessitates suitable regularization terms, such as Tikhonov or non-negative fused lasso (NFL) regularization, to stabilize the solution. While NFL regularization offers clearer edge information than Tikhonov regularization, it carries a biased estimate of the l_1 penalty, leading to an underestimation of the reconstructed concentration and adversely affecting the quantitative properties. In this paper, a new nonconvex regularization method including min-max concave (MC) and total variation (TV) regularization is proposed. This method utilized MC penalty to provide nearly unbiased sparse constraints and adds the TV penalty to provide a uniform intensity distribution of images. By combining the alternating direction multiplication method (ADMM) and the two-step parameter selection method, a more accurate quantitative MPI reconstruction was realized. The performance of the proposed method was verified on the simulation data, the Open-MPI dataset, and measured data from a homemade MPI scanner. The results indicate that the proposed method achieves better image quality while maintaining the quantitative properties, thus overcoming the drawback of intensity underestimation by the NFL method while providing edge information. In particular, for the measured data, the proposed method reduced the relative error in the intensity of the reconstruction results from 28% to 8%.**

Index Terms—**ADMM, magnetic particle imaging, min-max concave, nonconvex regularization, quantitative reconstruction.**

Tao Zhu, Lin Yin, Zechen Wei, and Xin Yang are with the CAS Key Laboratory of Molecular Imaging, Beijing Key Laboratory of Molecular Imaging, Institute of Automation, Beijing 100190, China, and also with the School of Artificial Intelligence, University of Chinese Academy of Sciences, Beijing 100190, China (e-mail: zhutao2020@ia.ac.cn; yinlin2016@ia.ac.cn; weizechen2019@ia.ac.cn; xin.yang@ia.ac.cn).

Jie He is with the Key Laboratory of Big Data-Based Precision Medicine, Ministry of Industry and Information Technology, the School of Engineering Medicine, and the School of Biological Science and Medical Engineering, Beihang University, Beijing 100190, China (e-mail: jieh@buaa.edu.cn).

Jie Tian is with the CAS Key Laboratory of Molecular Imaging, Institute of Automation, Beijing Key Laboratory of Molecular Imaging, Key Laboratory of Big Data-Based Precision Medicine, Ministry of Industry and Information Technology, the School of Engineering Medicine, and the School of Biological Science and Medical Engineering, Beihang University, Beijing 100190, China, and also with the National Key Laboratory of Kidney Diseases, Beijing 100853, China (e-mail: tian@ieee.org).

Hui Hui is with the CAS Key Laboratory of Molecular Imaging, Beijing Key Laboratory of Molecular Imaging, Institute of Automation, Beijing 100190, China, also with the School of Artificial Intelligence, University of Chinese Academy of Sciences, Beijing 100190, China, and also with the National Key Laboratory of Kidney Diseases, Beijing 100853, China (e-mail: hui.hui@ia.ac.cn).

Digital Object Identifier 10.1109/TMI.2024.3383468

I. INTRODUCTION

MAGNETIC particle imaging (MPI) is a novel imaging modality first introduced by Gleich and Weizenecker in 2005 [1]. The spatial distribution of superparamagnetic iron oxide nanoparticles (SPIONs) can be reconstructed by utilizing the nonlinear magnetization response of SPIONs in alternating magnetic fields. As a noninvasive imaging method, MPI has highly sensitive and quantitative characteristics, which makes it promising for use in biological applications [2], [3], [4], [5], [6], [7]. Examples include drug delivery [2], visualization of vascular interventions [3], in vivo tracking of minute numbers of cells [4], and quantitative monitoring of tumor immunotherapy [5].

In MPI reconstruction, the spatial distribution of SPIONs can be decoded using a system-matrix-based approach. However, because the system matrix-based inverse problem is ill posed, a direct solution is unstable [8], [9]. Therefore, regularization, such as the Tikhonov penalty [10], nonnegative Garrote penalty [11], lasso penalty [12], nonnegative fused lasso (NFL) regularization [13], and elastic net regularization [14], is required to stabilize image reconstruction. Among these, the Tikhonov penalty is the most widely used regularization approach in MPI reconstruction [8], [10]. Combined with the Kaczmarz method, this enables a fast solution using row iterations. However, Tikhonov regularization has a limited ability to suppress noise and over-smooth images. Considering the sparse and piecewise constant distribution of magnetic particles, Storath et al. introduced NFL regularization by combining the l_1 and total variation (TV) norms [13]. This method can effectively suppress noise and maintain edge information in an image. Although the l_1 norm in NFL regularization is the most effective sparsity-induced term among convex

regulars, it is a biased estimate that tends to underestimate the true solution [15], [16]. This reduces the concentration of magnetic particles in the reconstructed images and weakens the advantage of MPI in terms of quantitative imaging.

To reduce the bias effect while maintaining sparsity, nonconvex regularizations, such as the smoothly clipped absolute deviation [17], log sum penalty [18], l_q-norm penalty ($0 < q < 1$) [19], and min-max concave (MC) penalty [20], have been introduced. The optimization properties of nonconvex regularization are more similar to those of the l_1-norm penalty than to those of the ideal l_0-norm penalty. Therefore, nonconvex regularization can improve the reconstruction accuracy and suppress the bias effect. Several techniques can be adopted to solve nonconvex optimization problems, such as the Bayesian compressive sensing [21], focal underdetermined system solutions [22], and iterative reweighted least squares [23] methods. However, these methods are not suitable for solving large-scale problems because of their high computational costs. Selesnick proved that a nonconvex optimization problem has a simple closed-form solution for proximal operators when the penalty satisfies specific conditions (such as the MC penalty) [24], which can accelerate the solution of nonconvex optimization problems. Furthermore, when more than one penalty is included in the regular term, the alternating direction method of multipliers (ADMM) is suitable. It simplifies the solution by decomposing a complex problem into several simple subproblems. Recently, ADMM reconstruction has been applied to MPI reconstruction and has exhibited good performance [25].

In this paper, we propose a new regularization term for MPI reconstruction that enables accurate MPI concentration reconstruction, achieving better image quality while maintaining the quantitative advantages of MPI. The contributions of this work are as follows: (i) a regularization that better matches the quantitative reconstruction of MPI is proposed; (ii) a suitable solution method and a two-step parameter selection method are designed, which simplify the selection process of multiple parameters and realize the fast solution of the objective function; and (iii) the effectiveness and advantages of the proposed method are verified through experiments using Open-MPI data and measured data.

To evaluate the performance of the proposed method, we used different phantoms, including stenosis, overlapping ellipses with different intensities, and vascular trees. Nonnegative Tikhonov regularization utilizing the Kaczmarz method and NFL regularization employing the forward-backward (FB) method were applied for comparison. The results demonstrated that the proposed nonconvex regularization solved with ADMM could provide precise intensity estimation while maintaining edge information.

II. FORWARD AND RECONSTRUCTION PROBLEMS IN MPI

A. Forward Problem

The forward problem of MPI involves establishing of a mathematical model of the process in which the nonlinear magnetization of SPIONs is excited by an alternating magnetic field and signal encoding within the signal chain. Assuming that the particles are always in thermal equilibrium, the nonlinear magnetization properties of SPIONs can be modeled by the Langevin function $L(.)$, expressed as:

$$M(r, t) = c(r)\bar{M}(r, t) = c(r)m\mathcal{L}(\xi)e_H,$$
$$\mathcal{L}(\xi) = \left(coth(\xi) - \frac{1}{\xi}\right),$$
$$\xi = \frac{\mu_0 m||H(r, t)||_2}{kBT}, \quad (1)$$

where $c(r)$ is the concentration of SPIONs at position r, Ms is the magnetization of the particles at unit concentration, m is the magnetic moment, and $e_H = H(r, t)/||H(r, t)||_2$ is the normalized direction of the magnetic field strength $H(r, t)$. μ_0 denotes the permeability of vacuum, k_B denotes the Boltzmann constant and T is the temperature.

Signal encoding is based on the MPI signal chain. The relationship between the particle distribution c and the induced voltage can be expressed as:

$$u(t) = -\mu_0 \int \Omega \frac{\partial}{\partial t}\bar{M}(r, t)\, p(r)\, c(r)\, dr \quad (2)$$

where $p(r)$ is the sensitivity of receive coils. Using the Fourier transform and discretization, the model can be expressed as:

$$Sc = u \quad (3)$$

where $S \in \mathbb{C}^{M \times N}$ denotes the system matrix, M is the number of frequencies, and N is the number of discrete points. $c = [c_1, c_2, \ldots, c_N]^T \in \mathbb{R}^{N \times 1}$ denotes the particle concentration at N positions and $u = [u_1, u_2, \ldots, u_N]^T \in \mathbb{C}^{M \times 1}$ denotes the induced voltage signal in the frequency domain.

B. Reconstruction Methods

The reconstruction problem of the MPI is aimed at solving the linear problem (3). However, this approach can only acquire an approximate optimal solution because the system matrix of the MPI is ill-conditioned, which means that the singular values decay rapidly, and a small noise disturbance has a significant impact on the reconstruction results [26]. Therefore, a regularization term is typically added when solving an inverse problem. The Tikhonov and NFL regularization are the two most well-known types of regularization. The former is the most widely used penalty in MPI reconstruction, whereas the latter is a state-of-the-art penalty.

1) Nonnegative Tikhonov Regularization: The objective function of the nonnegative Tikhonov regularization is:

$$\min_{c \geq 0} \frac{1}{2}\|Sc - u\|_2^2 + \lambda\|c\|_2^2 \quad (4)$$

where $\|\cdot\|_2^2$ denotes the Euclidean norm. Equation (4) is a typical least-squares optimization problem that can be solved using singular value decomposition [27] and conjugate gradient [28] methods. However, the computational cost is high when the system matrix is large.

Weizenecker introduced the Kaczmarz method to obtain a fast solution, which is calculated using row iterations and requires only a few iterations to reach convergence [29].

In addition, a weighting matrix was employed to weigh the rows of the system matrix by utilizing the row energy. Preprocessing can improve image quality and shorten the reconstruction time [10]. Because of its short convergence time and good robustness, nonnegative Tikhonov regularization based on the Kaczmarz method is popular in practice [8], [30].

2) NFL Regularization: To improve the image quality, Storath introduced a near-isotropic TV norm to consider prior neighborhood structures while using the l_1-norm to induce sparsity [13]. The objective function can be expressed as:

$$\min_{c \geq 0} \frac{1}{2} \|Sc - u\|_2^2 + \lambda_1 \|c\|_1 + \lambda_2 TV_{near-iso}(c), \quad (5)$$

where $\|\cdot\|_1$ denotes the l_1-norm of c and $TV_{near-iso}(\cdot)$ denotes the near-isotropic TV norm regularization. Compared to nonnegative Tikhonov regularization, this method suppresses more noise and preserves better edge information. Furthermore, the FB algorithm can avoid excessive computational costs, even if the objective function is complex.

III. PROPOSED MC REGULARIZATION METHOD

The two aforementioned popular MPI reconstruction methods have their own advantages and disadvantages in terms of reconstructed image quality. Tikhonov-based reconstruction can achieve fast and relatively high-quality reconstruction. However, the l_2-norm penalty cannot provide sufficient noise suppression in the case of high signal noise, and it smooths the edges of magnetic particles, which is not conducive to obtain detailed information. The NFL method can achieve stronger noise suppression and edge recovery. However, its ability to predict particle concentration is not sufficiently accurate, which affects the quantitative properties of MPI imaging. This situation may be caused by the biased effect of the l_1-norm. Accordingly, we propose the use of low-bias sparse regularization to improve the quality of MPI-reconstructed images and ensure quantitative accuracy while guaranteeing reconstruction quality.

A. Nonconvex Hybrid Penalty Combining MC and TV Regularization

The objective function based on the proposed method is as follows:

$$\min_{c \geq 0} \lambda_{TV} \|c\|_{TV} + \lambda_{MC} \|c\|_{MC}$$
$$\text{s.t.} \|Sc - u\|_2^2 \leq \varepsilon, \quad (6)$$

where $|\cdot|_{TV}$ denotes the isotropic TV norm, $|\cdot|_{MC}$ denotes the MC penalty norm, and $\varepsilon \geq 0$ depends on the noise variance. λ_{TV} and λ_{MC} are the regularization parameters. The MC function used in this study can be expressed as:

$$\|x\|_{MC} = \|x\| - S_b(x),$$
$$S_b(x) = \min_{v \in \mathbb{R}} \left(\|v\| + \frac{1}{2}b^2(x-v)^2 \right) \quad (7)$$

where b is the scaling parameter and v is an intermediate parameter.

The MC regularization-based objective function is given as

$$\min_X \frac{1}{2} \|Y - X\|_2^2 + \lambda \|X\|_{MC}, \quad (8)$$

here, $Y = [Y_1, \ldots, Y_i, \ldots, Y_m]^T \in \mathbb{R}^m$ and $X = [X_1, \ldots, X_i, \ldots, X_m]^T \in \mathbb{R}^m$. λ is the regularization parameter. The objective function can be equally written in element form as

$$\frac{1}{2}(Y_i - X_i)^2 + \lambda |X_i|_{MC}$$
$$= \frac{1}{2}(Y_i - X_i)^2 + \lambda \left(|X_i| - \min_v \left(|v| + \frac{1}{2}b^2(X_i - v) \right) \right)$$
$$= \frac{1}{2}\left(1 - \lambda b^2\right) X_i^2 + \lambda |X_i|$$
$$+ \max_v \left(\frac{1}{2}\left(Y_i^2 - 2X_i Y\right) - \lambda |v| - \frac{1}{2}\lambda b^2\left(v^2 - 2X_i v\right) \right), \quad (9)$$

In this case, the objective function is convex when $1 - \lambda b^2 \geq 0$. Let $\theta = 1/b^2$. The firm threshold function is given as follows, with $\lambda > 0$ and $\theta > 0$ [24]:

$$firm(Y_i, \lambda, \theta) = \begin{cases} 0, & |Y_i| \leq \lambda \\ \theta\lambda \dfrac{|Y_i| - \lambda}{\theta\lambda - \lambda} sign(Y_i), & \lambda < |Y_i| \leq \theta\lambda \\ Y_i, & |Y_i| > \theta\lambda, \end{cases} \quad (10)$$

The l_1-norm problem is expressed as:

$$\min_X \frac{1}{2} \|Y - X\|_2^2 + \lambda \|X\|_1 \quad (11)$$

The solution can be calculated using the soft-threshold function:

$$soft(Y, \lambda) = \begin{cases} 0 & , |Y_i| < \lambda \\ sign(Y_i)(|Y_i| - \lambda), & |Y_i| \geq \lambda, \end{cases} \quad (12)$$

where $sign(\cdot)$ is a symbolic function.

The derivation of the l_1-norm and MC penalty is formulated as:

$$\lambda |X_i|'_{l1} = \lambda \cdot sign(X_i)$$
$$\lambda |X_i|'_{MC} = \begin{cases} \lambda(sign(X_i) - \dfrac{X_i}{\theta}), & |X_i| \leq \theta \\ 0, & |X_i| > \theta, \end{cases} \quad (13)$$

A comparison of the l_0-norm, l_1-norm and MC penalty demonstrates the rationale for using the MC penalty (see Fig. 1). As shown in Fig. 1(a), a comparison of the penalties and threshold functions reveals that that the MC penalty is a more accurate estimator of the ideal l_0-norm penalty than other penalties. In addition, a comparison of the derivatives shows that the MC penalty begins penalizing by applying the same rate as the l_1-norm penalty. However, the l_1-norm penalty tends to over-penalize which introduces estimation bias when it deviates from zero. In contrast, the MC penalty relaxes the penalization rate to zero and reduces the bias. Therefore, the reconstruction results obtained using the MC penalty can suppress the bias existing in the l_1-norm penalty.
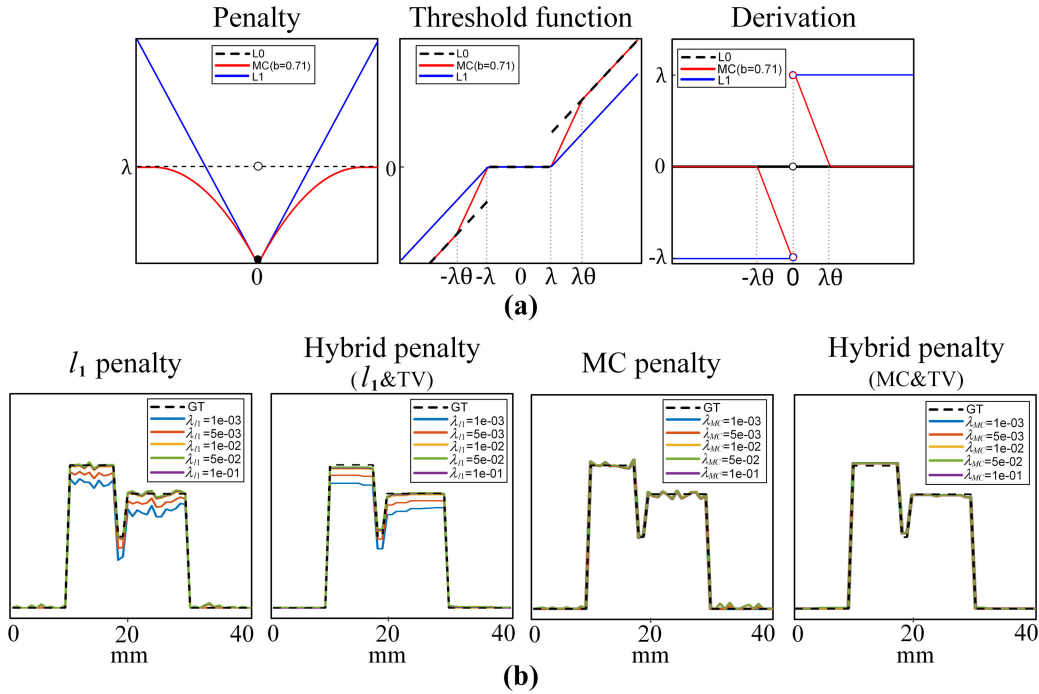
Fig. 1. Comparison of the l_0-norm, l_1-norm, and MC penalty functions. (a) Comparison of the l_0-norm, l_1-norm, and MC penalty; (b) comparison of the 1D reconstruction results for l_1, the MC and the corresponding TV hybrid penalty. The simulated data were used in experiments and the phantom have concentration varied in the middle region. The ordinate indicates the particle concentration in linear and arbitrary scales. The reconstruction results show that the MC penalty is effective at suppressing the bias introduced by the l_1 penalty. Furthermore, by adding TV regularization, the concentration distribution of the results becomes more uniform. For both hybrid reconstructions in (b), the parameter of the TV regularization is 0.02.

Moreover, considering the continuity and uniformity of the SPION distribution in MPI images, TV regularization is also applied in our method to ensure a uniformly distributed intensity in the reconstructed results (see Fig. 1(b)). Based on the above prior knowledge, the proposed optimization method involving MC and TV regularization is reasonable.

B. Nonconvex Hybrid Penalty Based on the ADMM

Considering the advantages of the ADMM in solving large-scale sparse models, we apply the ADMM to solve the function (6) while utilizing the hybrid cost function form, LU decomposition, firm threshold, and Chambolle projections to speed up convergence. The detailed derivation process is as follows.

To solve the optimization problem of the two separable objective functions, we employ an ADMM with a hybrid cost function. The variable splitting scheme [31], [32] is employed to convert the function (6) into the following form:

$$\min_x f_1(c) + f_2(z)$$
$$\text{s.t. } Pc + Qz - s = 0,$$
$$f_1(c) = 0,$$
$$f_2(z) = \iota_{E(\varepsilon, I, u)}\left(z^0\right) + \lambda_{TV}\|c\|_{TV} + \lambda_{MC}\|c\|_{MC}. \quad (14)$$

Here, $z = [z^0, z^1, z^2]^H$, $P = [S^H I\ I]^H$, $Q = -I$ and $s = 0$ are the introduced variables. $[\cdot]^H$ is the conjugate transpose of the matrix, $\iota_{E(\varepsilon, I, u)}\left(z^0\right)$ accounts for the indicator function associated with the data fidelity constraint $\|Sc - u\|_2 \leq \varepsilon$, and I is an identity matrix.

To improve the robustness of the algorithm, the augmented Lagrangian method is adopted. This method does not require strict convexity or finiteness of the objective function and can realize fast iterative convergence of the ADMM. The ADMM steps include the updating of variables c, z, and the Lagrange multiplier $d = [d^0, d^1, d^2]^T$, as shown in (15)–(21). Parameter β is the penalty coefficient of the Lagrange function [33].

$$c_{k+1} = \left(2I + S^H S\right)^{-1}\left[\sum_{i=1}^{2}\left(d_k^i + z_k^i\right) + S^H\left(d_k^0 + z_k^0\right)\right] \quad (15)$$

$$z_{k+1}^0 = \arg\min_{z^0} \iota_{E(\varepsilon, I, u)}\left(z^0\right) + \frac{\beta}{2}\left\|Sc_{k+1} - z^0 - d_k^0\right\|_2^2 \quad (16)$$

$$z_{k+1}^1 = \arg\min_{z^1} \|z_{k+1}\|_{TV} + \frac{\beta}{2\lambda_{TV}}\left\|c_{k+1} - z^1 - d_k^1\right\|_2^2 \quad (17)$$

$$z_{k+1}^2 = \arg\min_{z^2} \|z_{k+1}\|_{MC} + \frac{\beta}{2\lambda_{MC}}\left\|c_{k+1} - z^2 - d_k^2\right\|_2^2 \quad (18)$$

$$d_{k+1}^0 = d_k - Sc_{k+1} + z_{k+1}^0 \quad (19)$$
$$d_{k+1}^1 = d_k - Sc_{k+1} + z_{k+1}^1 \quad (20)$$
$$d_{k+1}^2 = d_k - c_{k+1} + z_{k+1}^2 \quad (21)$$

By solving the above ADMM subproblems, (14) can be calculated.

C. Fast Solution of Subproblems

In (15), the direct calculation of the inversion term $\left(2I + S^H S\right)^{-1}$ may be time- and memory-consuming owing

to the high matrix dimension. In particular, for 3D-MPI reconstruction, the number of pixels N is usually much greater than the frequency number M. Therefore, we adopted the LU decomposition scheme prior to inversion to avoid the direct inversion operation as:

$$c = \begin{cases} U_1^{-1} L_1^{-1} q & , M \leq N \\ \dfrac{q}{2} - \dfrac{S^H U_2^{-1} L_2^{-1} Sq}{4} & , M > N, \end{cases} \quad (22)$$

here $L_1, L_2 \in \mathbb{C}^{N \times N}$ is a lower triangular matrix and $U_1, U_2 \in \in \mathbb{C}^{N \times N}$ is an upper triangular matrix. $L_1 U_1 = 2I + S^H S$, $L_2 U_2 = SS^H/2 + I$, and $q_1 = \sum_{i=1}^{2} (d_k^i + z_k^i) + S^H (d_k^0 + z_k^0)$.

Equation (16) can be solved using the Moreau proximal map $\Psi_{\iota_{E(\varepsilon, I, u)}}(Sc_{k+1} - d_k^0)$, and it can be easily calculated by the orthogonal projection of $Gc_{k+1} - d_k^0$ on the closed ε-radius ball centered at u. The solution is as follows [33]:

$$\Psi_{\iota_{E(\varepsilon, I, u)}} (\delta) = u + \begin{cases} \varepsilon \dfrac{\delta - u}{\|\delta - u\|_2}, & if \|\delta - u\|_2 > \varepsilon \\ \delta - u, & if \|\delta - u\|_2 \leq \varepsilon \end{cases}$$
$$\delta = Sc_k - d_k^0, \quad (23)$$

Similarly, the Moreau proximal form of (17) can be described as $\Psi_{\|\cdot\|_{TV}}(c_{k+1} - d_k^1, \frac{\lambda_{TV}}{\mu})$ and the optimization function is

$$\min_z \frac{1}{2} \|(c - d) - z\|_2^2 + \frac{\lambda_{TV}}{\beta} \|X\|_{TV}, \quad (24)$$

Here, we adopt an isotropic TV norm that can be quickly calculated using Chambolle projections as follows [34]:

$$z = sign(c - d) \left(|c - d| - \frac{\lambda_{TV}}{\beta} div(p^{t+1}) \right)$$
$$p^{t+1} = \frac{p^t + \tau \left(\nabla \left(div\, p^t - \frac{|c-d|}{\lambda_{TV}/\beta} \right) \right)}{max \left\{ 1, \left| p^t + \tau \left(\nabla \left(div\, p^t - \frac{|c-d|}{\lambda_{TV}/\beta} \right) \right) \right| \right\}}, \quad (25)$$

where $p = (p^1, p^2)$ is the dual variable of z, ∇ denotes the gradient operator, div denotes the divergence operator, and τ represents the iteration step size, which is usually set to $\tau = 0.248$ [34].

Equation (18) can be formulated as an MC-based optimization problem:

$$\min_z \frac{1}{2} \|(c - d) - z\|_2^2 + \frac{\lambda_{MC}}{\beta} \|X\|_{MC}, \quad (26)$$

To maintain the convexity of the subproblem, $\lambda_{MC} \leq \beta\theta$ is needed, and it can be solved using (10).

D. Parameter Selection

The complete procedure is shown in Algorithm 1. In the ADMM solution, five parameters exist: ε, β, θ, λ_{TV}, and λ_{MC}. It is unrealistic to search for the optimal parameters directly; therefore, some simplifications are used in the selection of the parameters. Here, the parameter θ is set to 2 to maintain the convexity of the MC constrained subproblem and to enable the firm threshold function (10) to realize the fast solution. The data fidelity term ε is related to the noise level during scanning. The higher the noise, the larger ε should be set to provide greater noise suppression. The penalty parameter β

Algorithm 1 ADMM with minimax concave & TV regularization for MPI

1: **Input**: Measured data $u \in \mathbb{C}^{M \times 1}$, system matrix $S \in \mathbb{C}^{M \times N}$, multiplier $d = [d^0, d^1, d^2] \in \mathbb{C}^{M \times 3}$, regularization parameters $\lambda_{TV}, \lambda_{MC}, \varepsilon, \beta \geq 0$ and maximum iterations K_{MAX}.
2: **Output**: Reconstructed data $c \in \mathbb{C}^{N \times 1}$.
3: **Repeat:**
4:     Calculate c_{k+1} by (21);
5:     $z_{k+1}^0 = \Psi_{\iota_{E(\varepsilon, I, u)}}(Sc_{k+1} - d_k^0)$;
6:     $d_{k+1}^0 = d_k^0 - Sc_{k+1} + z_{k+1}^0$;
7:     $z_{k+1}^1 = \Psi_{\|\cdot\|_{TV}}(c_{k+1} - d_k^1, \frac{\lambda_{TV}}{\beta})$;
8:     $d_{k+1}^1 = d_k^1 - c_{k+1} + z_{k+1}^1$;
9:     $z_{k+1}^2 = \Psi_{\|\cdot\|_{MC}}(c_{k+1} - d_k^2, \frac{\lambda_{MC}}{\beta})$;
10:     $d_{k+1}^2 = d_k^2 - c_{k+1} + z_{k+1}^2$;
11:     $k = k + 1$;
12:    **Until** *stop criterion reached* **or** $k > K_{MAX}$;
13:    **Return** c

---

affects the convergence speed, and a proper β can reduce the solution time, which is detrimental to the fast convergence of the algorithm. The parameters $\lambda_{TV} > 0$ and $\lambda_{MC} > 0$ are the coefficients of the two regularizations used.

The parameter ε can be selected roughly based on the standard deviation (STD) of the noise by $\varepsilon = \gamma \cdot STD$, $\gamma > 0$. For the parameter β, without the support of a priori information, a suitable value for the parameter is difficult to set before iteration. Therefore, based on the residual balancing strategy [35], we use an adaptive method to automatically update β in iterations and adaptively select the appropriate β value:

$$\beta_{k+1} = \begin{cases} \tau_{incr}\beta_k & , \left\| r_p^k \right\|_2 > \kappa \left\| r_d^k \right\|_2 \\ \beta_k/\tau_{decr} & , \left\| r_d^k \right\|_2 > \kappa \left\| r_p^k \right\|_2 \\ \beta_k & , otherwise, \end{cases} \quad (27)$$

here, $\tau_{incr} > 1$, $\tau_{decr} > 1$ and $\kappa > 1$ are parameters. $r_p^k = Pc + Qz - c$ and $r_d^k = \beta P^T Q(z^k - z^{k-1})$ are refer to the primal and dual residuals, respectively at iteration k. In general, the selection of multiple parameters is simplified into two steps in our work. First, the ε is selected according to the standard deviation of the noise, and the penalty parameter β is selected with the adaptive method as shown in (27). Second, λ_{TV} and λ_{MC} are screened in (0, 1), where $\lambda_{TV} + \lambda_{MC} = 1$ is satisfied. The algorithm is terminated when the maximum number of iterations or the stopping condition is reached. We set the stop condition as the relative change in the result between two iterations that was lower than the tolerance, described as $\|c_{k+1} - c_k\|/\|c_k\| + 10^{-4} < tol$. All the aforementioned parameters were chosen to achieve the set tolerance or maximum number of iterations.

IV. EXPERIMENT AND RESULTS

A. Simulation Experiment Setup

We implemented all the algorithms in MATLAB R2018b and simulated the data according to $u = Sc + \eta$, where c
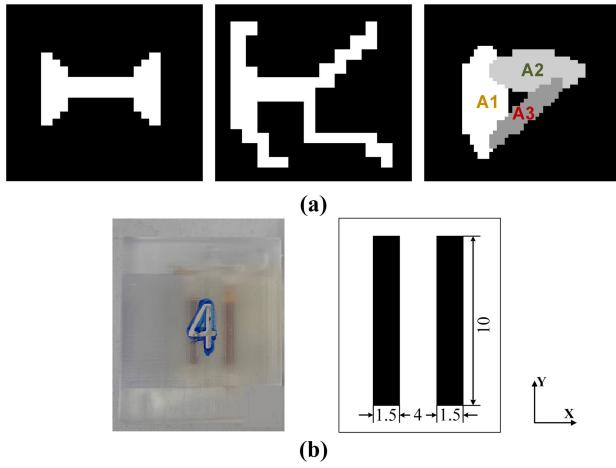
Fig. 2. Phantoms used in our study. (a) Phantoms used in the simulation study, including the stenosis phantom (left), the vessel phantom with a plaque in the main vessel (middle), and the ellipses with different intensities (right, and the intensity in A1:1; A2:0.8; A3:0.6). (b) Phantom used in the real-world experiment. Bar phantom (left) and its schematic (right) used for the measurements (unit: mm).

denotes the ground truth of size $N = 51 \times 51$, $M = 9900$ is the number of frequency points, and η is Gaussian noise. Three different phantoms were built in the simulation: a stenosis phantom, a vessel phantom with plaque in the main vessel, and an overlapping elliptical phantom with multiple intensities [13] (see Fig. 2(a)). The stenosis phantom has a simple structure, whereas the vascular and elliptical models are more complex. Additionally, the overlapping elliptical phantom has a more complex concentration distribution. Considering the reconstruction and time consumption, we preset the stop condition for the methods used. For the nonnegative Tikhonov regularization method, we performed 10 iterations. For the NFL and proposed methods, we stopped the iterations when the tolerance was less than 1×10^{-3} or the number of iterations reached 40. The NFL method used the same parameter settings as those in the original study [13].

First, in order to verify the effectiveness of the proposed method under different structural complexity and concentration distribution complexity phantoms, reconstruction experiments were performed using the three designed phantoms and compared with the non-negative Tikhonov regularization and the NFL method. The data were corrupted by Gaussian noise with a 30dB signal-to-noise ratio (SNR) Subsequently, the profiles across the reconstructed results were extracted to compare the intensity distribution along the profiles.

Furthermore, for the quantitative reconstruction target in the paper, we focused on the overlapping elliptical phantom with multiple intensities. To compare the robustness of the algorithm under different noise levels, corrupted signals with SNR of 25 dB, 20 dB, and 15 dB were used. Error maps were used to visualize overall error, and the relative error between the reconstruction results and the ground truth in regions A1, A2, and A3 were calculated for quantitative comparison.

B. Open-MPI Dataset

To verify the feasibility of the proposed algorithm for the measured data, the system matrix and signal of phantoms in

the Open-MPI dataset were used to verify our method [36]. We selected a 2D MPI system matrix with 19^3 voxel scans using a 2D Lissajous trajectory. Because the measurements of the 19 planes are stitched together in the Open-MPI dataset, preprocessing is required when 2D sliced data are necessary. During data processing, frequency data with an SNR lower than three were discarded to obtain a system matrix of dimensions 824×19^3. The image was then sliced into 19 2D system matrices of dimensions 824×19^3, corresponding to the 19 planes scanned using a 2D Lissajous trajectory. Similarly, we sliced the measurement data to a size of 19,000 every 1000 times to obtain 19 signals, corresponding to 19 planes of data. Subsequently, a 2D system matrix of each plane with the corresponding phantom signals was obtained.

Experiments were conducted using shape and concentration phantoms from the dataset. After reconstruction using different methods, the absolute reconstructed intensities were compared using a shape phantom, and the accuracy of the concentration gradient was compared when multiple concentrations of particles were present in the field of view.

C. Measured Data

Furthermore, we validated the proposed algorithm by utilizing data measured using a prototype MPI scanner built in our laboratory [37]. The scanner was encoded based on the field-free point, and the Cartesian trajectory was used to construct a 2D measurement sequence (selection field gradient: $1.5\ Tm^{-1}\mu_0^{-1}$ in the x and y directions, drive field amplitude: $27\ Tm^{-1}\mu_0^{-1}$ in the x and y directions, excitation frequency: 25 kHz, scanning frequency: 20 Hz). A delta sample with dimensions of $2 \times 2 \times 1\ mm^3$ was used to measure the system matrix $S \in \mathbb{C}^{M \times N}$ (frequency component $M = 1.25 \times 10^6$, position $N = 121$). The background signal was measured at each position to reduce the effect of dynamic noise and was utilized for frequency selection. A bar phantom containing two rectangular cavities was employed for the measurements and imaging tests. The edge-to-edge distance between the two cavities was 4 mm. A schematic diagram and the dimensional size are shown in Fig. 2(b). As mentioned above, Tikhonov regularization, NFL regularization and the proposed method were utilized to reconstruct the images, and the results were compared using qualitative and quantitative metrics.

D. Evaluation Indices

We used the normalized root mean square error (NRMSE), peak signal-to-noise ratio (PSNR), and structural similarity index (SSIM) to evaluate the reconstruction quality, and the reconstruction time were recorded.

The NRMSE is used to scale the RMSE to the range of $(0, 1)$ and indicates the difference between the reconstructed image and the ground truth. The RMSE is defined as follows:

$$NRMSE = \frac{\sqrt{\frac{1}{M \times N}\sum_{i=1}^{M}\sum_{j=1}^{N}(I_R(i,j) - I_G(i,j))^2}}{\max(I_R(i,j)) - \min(I_R(i,j))}, \quad (28)$$

I_R and I_G denote the reconstructed and ground-truth images, respectively. $NRMSE \in [0, 1]$. A smaller value
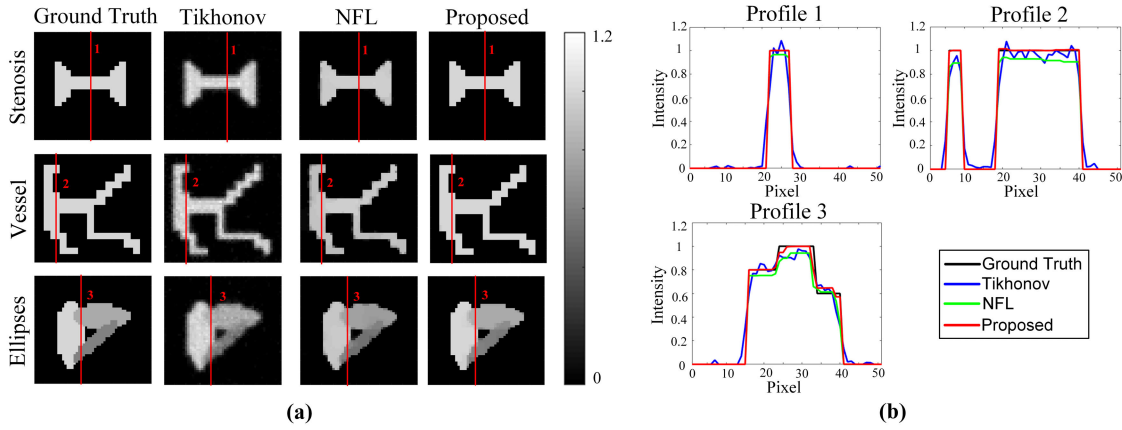
Fig. 3. Reconstruction results for phantoms. (a) Reconstructed images of the stenosis phantom (top), vessel phantom (middle), and elliptical phantom (bottom). (b) Intensity distribution along the profile. The profile of the stenosis phantom is column25, that of the vessel phantom in column10, and that of the elliptical phantom in column 21. (See Table I for a quantitative comparison, Table V for regularization parameters and Table VI for the computation time.)

TABLE I
QUANTITATIVE RESULTS OF THE PHANTOMS USED

		Stenosis	Vessel	Ellipses
SSIM ↑	Tikhonov	0.815	0.754	0.751
	NFL	0.989	0.973	0.968
	Proposed	**0.99**	**0.99**	**0.98**
PSNR ↑	Tikhonov	19.786	18.132	21.460
	NFL	28.153	23.796	25.803
	Proposed	**57.8**	**50.8**	**31.1**
NRMSE ↓	Tikhonov	0.092	0.124	0.085
	NFL	0.040	0.066	0.054
	Proposed	**0.001**	**0.003**	**0.028**

indicates better image quality. The PSNR is described as

$$PSNR = 10 \cdot log_{10}(\frac{MAX_I^2}{MSE}), \qquad (29)$$

MAX_I denotes the maximum intensity of the image.

The SSIM, which considers brightness, contrast, and structure, was used to evaluate the similarity between two images and was calculated as follows:

$$SSIM(I_R, I_G) = \frac{(2\mu_{I_R}\mu_{I_G} + c_1)(2\sigma_{I_R I_G} + c_2)}{(\mu_{I_R}^2 + \mu_{I_G}^2 + c_1)(\sigma_{I_R}^2 + \sigma_{I_G}^2 + c_2)}, \quad (30)$$

Here, μ_I and σ_I^2 are the mean and variance of an image, respectively. σ_{I_R} and σ_{I_G} are the covariance of I_R and I_G, respectively.

V. RESULTS

A. Reconstruction Comparison

The reconstruction results for the simulated phantoms are shown in Fig. 3, and the corresponding quantitative results are listed in Table I. Considerable background noise exists in the reconstruction results of the Tikhonov regularization. Moreover, the edges of the phantom were blurred, making it difficult to identify sharp edges.

For the NFL and proposed methods, the edges in the reconstructed images were sharper, and the intensity distribution inside the phantom was more uniform because of the TV norm. However, our proposed method can achieve better
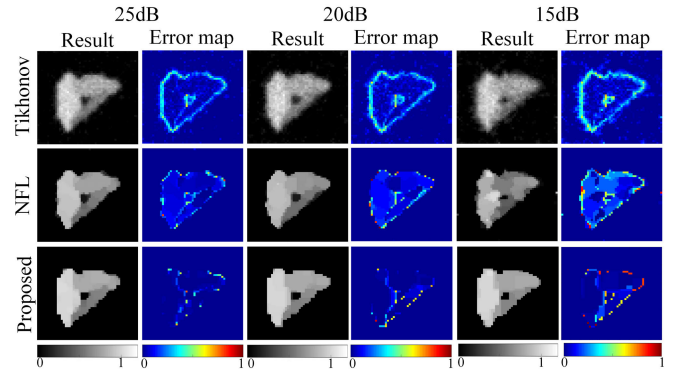

Fig. 4. Visualization reconstructions and error maps of the elliptical phantom with different intensities. (See Table II for a quantitative comparison, Table V for the regularization parameters and Table VI for the computation time.)

reconstruction than the other methods, and it yields the most accurate recovery of the shape of the phantom among the three methods. Furthermore, as shown in Table I, the SSIM, PSNR, and NRSME of the reconstructed results obtained using the proposed method are superior to those of the results acquired by utilizing other methods. In addition, the comparison of the intensity distributions on the profile shows that the NFL regularization clearly underestimates the intensity compared to the ground truth, whereas the proposed method can could compensate for this drawback better, as shown in Fig. 3(b).

B. Error Comparison

To assess the ability to recover the intensity more accurately, we also reconstructed a multigray elliptical phantom with different intensities in each elliptical region, as shown in Fig. 2. The results are presented in Fig. 4 and Table II. In Fig. 4, the NFL method and proposed method both maintain the edges clearly. However, the error map in Fig. 4 reveals the inferiority of the NFL method. The intensity inside the ellipses is underestimated owing to the bias effect of the l_1-norm. A clearer error map obtained using the proposed method indicates that this approach can provide a more accurate reconstruction. The relative errors of the reconstructed

TABLE II
MEAN VALUE AND RELATIVE ERROR OF THE DIFFERENT
AREAS IN THE ELLIPTICAL PHANTOM

	Method	SNR		
		25	20	15
A1	Tikhonov	0.922/7.8%	0.884/11.6%	0.85/15%
	NFL	0.915/8.5%	0.839/16.1%	0.789/21.1%
	Proposed	**0.983/1.7%**	**0.978/2.2%**	**0.962/3.8%**
A2	Tikhonov	0.759/5.1%	0.737/7.8%	0.7/12.5%
	NFL	0.732/8.5%	0.702/12.2%	0.592/26%
	Proposed	**0.785/1.9%**	**0.796/0.5%**	**0.765/4.4%**
A3	Tikhonov	0.573/4.5%	0.554/7.6%	0.541/9.8%
	NFL	0.558/7%	0.498/17%	0.488/18.6%
	Proposed	**0.601/1.2%**	**0.602/0.5%**	**0.628/4.7%**

· The metrics in the table are displayed as (average intensity in each area ↑) / (Relative error ↓). The ground truths of area A1, A2, and A3 are 1, 0.8, and 0.6.

results and ground truths were calculated and are presented in Table II. The error values were reduced to within 5%.

To evaluate the ability to recover the grayscale values more accurately, we focused on an elliptical phantom with different intensities. With SNR of 25 dB, 20 dB, and 15 dB, we used Tikhonov, NFL, and the proposed regularization to reconstruct the signal and plot the error map, as depicted in Fig. 4. In addition, the average intensity in each elliptical region and the relative error were calculated and are presented in Table II. The error maps and the results in Table II reveal that although the NFL method can reconstruct the edge information more clearly, it underestimates the value inside each ellipse, which undermines the quantitative nature of MPI imaging, and its relative error is even greater than that of the Tikhonov method. The clearer error maps of the proposed method show that our method can provide more accurate reconstructions. The error can be suppressed to within 5%, thereby maintaining better quantitative properties.

C. Open-MPI Data Experiment

According to the results of our simulation experiments (Fig. 3 and Fig. 4), although the reconstruction results based on the Tikhonov penalty have the problem of over-smoothing, the intensity recovery is relatively accurate. Therefore, the intensity reconstructed using the Tikhonov penalty was used as a reference.

Fig. 5(a) shows the reconstruction results for the shape phantom in the Open-MPI dataset, and Fig. 5(b) displays the intensity distribution along the profile. For the Tikhonov regularization, the reconstruction results tend to converge to a maximum intensity of a few pixels and then become smooth (particularly in Profile 2 in Fig. 5(b)), which does not correspond to a uniform distribution of magnetic particles in the actual phantom cavity. For the NFL and proposed regularization method, as shown in Fig. 5(b), a stable region of intensity exists in the middle part along profile 2, which matches the actual situation. However, if the Tikhonov-based reconstruction results are taken as an approximation of the ground truth, Fig. 5(b) clearly shows that NFL regularization provides images with a significant intensity underestimation problem.
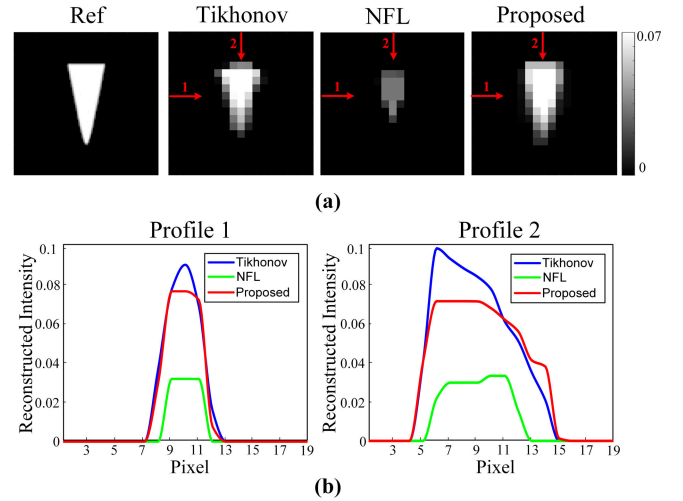

Fig. 5. Reconstruction of phantom shape using Open-MPI data. (a) Visualization results of the phantom shape and (b) intensity distribution along the profile given in (a). The data in (b) were interpolated. (See Table V for the regularization parameters and Table VI for the computation time.)
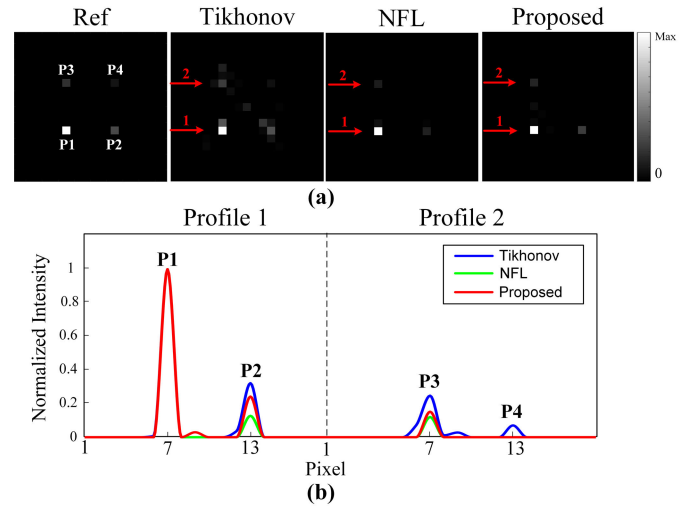

Fig. 6. Reconstruction of the concentration phantom in the Open-MPI dataset. (a) Visualization results. (b) Normalized intensity distribution along the profile (the profile is denoted by the red line in (a), and the arrow indicates the direction). And the data in (b) were interpolated. (See Table III for the quantitative results, Table V for the regularization parameters and Table VI for the computation time).

Furthermore, although NFL regularization provides clear edges, the reconstructed image has only a central part, with the pixels filled by particles. Pixels that were not completely filled with particles were discarded during reconstruction. Our proposed regularization can suppress the intensity underestimation problem and reduce the over-sparsity problem of NFL regularization. Moreover, the central part of the results reconstructed using our regularization method exhibited a uniform intensity distribution (Profile 2 in Fig. 5(b)).

Fig. 6(a) shows the reconstruction results of the concentration phantom in the Open-MPI dataset, and Fig. 6(b) displays the intensity distribution along the profile that passes through four different concentrations (P1, P2, P3, and P4). To compare the concentration gradients reconstructed using different penalties more clearly, the intensity along the profiles was
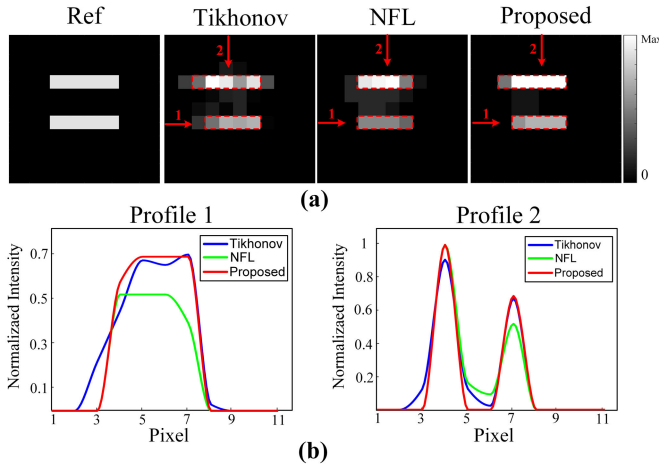
Fig. 7. Reconstruction was performed the data measured by a homemade MPI scanner. The intensity of the reconstructed images was normalized to [0,1]. (a) Reconstructed results, where the dashed red boxes in the images indicate the reconstructed rods (b) Intensity distribution along the profile given in (a), where the arrow shows the direction. (See Table IV for the quantitative comparison, Table V for the parameters used and Table VI for the computation time).

TABLE III
QUANTITATIVE RESULTS OF THE CONCENTRATION PHANTOM

	P1	P2	P3	P4
Ref	1	0.295	0.196	0.087
Tikhonov	1	0.322/9.2%	0.247/26.0%	0.070/19.5%
NFL	1	0.127/57.0%	0.120/38.8%	0/ NA
Proposed	1	0.242/18.0%	0.151/22.9%	0/NA

The data in the table are shown as the normalized intensity/relative error. The reference data are calculated from the Open-MPI dataset. The relative error was calculated by dividing bias intensity by Ref intensity. For P4, the results of the NFL method and the proposed method are 0, and the relative error is denoted by NA (Not Applicable).

normalized to [0,1]. Fig. 6(b) shows that the reconstruction results of the NFL method significantly underestimate the reconstruction intensity at points P2 - P4. And, as shown in Table III, the signal intensities of P2 and P3 in the results of the NFL method are close, which does not match the concentration ratios in the Open-MPI dataset. In contrast, the results of the proposed method reduce the relative error (shown in Table III), and the concentrations of the P2 and P3 points show a gradient decreasing trend, which is consistent with the setup in the Open-MPI dataset.

D. Measurement Data Experiment

For the data measured by the homemade MPI scanner, frequency points were selected using the SNR of each frequency [38]. Frequency points with an SNR > 10 dB were selected, and the number of filtered frequencies was 29. The images reconstructed using different regularizations are shown in Fig. 7(a). For Tikhonov regularization, the noise suppression is insufficient, leading to unclear reconstruction results. For the NFL and proposed regularization methods, two stripe distributions of magnetic particles can be clearly distinguished in the image. However, in the quantitative comparisons shown in Table IV, the concentration ratios of the two bars reconstructed by the NFL method deviate from the Ref value, whereas the ratios of the proposed method are closer to the Ref value

TABLE IV
QUANTITATIVE RESULTS OF THE BAR PHANTOM

	Ref	Tikhonov	NFL	Proposed
Bar1:Bar2	1:1	1:0.81	1:0.58	1:0.74
Absolute Error	/	19%	42%	26%
Relative Error	/	/	28%	8%

The value was calculated by the ratio of the mean values of the intensities in the selected dashed box in Fig. 7(a). Absolute errors were calculated based on the value of Ref, and relative errors were calculated based on the Tikhonov reconstruction result.

TABLE V
REGULARIZATION PARAMETERS FOR THE RECONSTRUCTED RESULTS

		Tikhonov	NFL		Proposed			
		λ	λ_1	λ_2	ε	β	λ_{TV}	λ_{MC}
Phantom experiment (Fig. 3)	stenosis	1.28	0.041	0.023	1.04	3.13	0.20	0.80
	vessel	0.74	0.040	0.025	1.40	3.13	0.20	0.80
	ellipses	0.35	0.055	0.021	1.10	3.13	0.30	0.70
Ellipses phantom experiment (Fig. 4)	25 dB	0.49	0.035	0.017	2.24	4.20	0.20	0.80
	20 dB	0.88	0.055	0.021	3.21	3.60	0.15	0.85
	15 dB	1.34	0.090	0.042	5.20	2.86	0.20	0.80
Open-MPI Shape phantom experiment (Fig. 5)		1×10^{-5}	0.25	2×10^{-3}	0.40	39.6	0.5	0.5
Open-MPI Resolution phantom experiment (Fig. 6)		2×10^{-7}	1×10^{-4}	1×10^{-4}	0.25	140	0.06	0.94
Measured data experiment (Fig. 7)		1×10^{-2}	0.26	0.05	0.3	7.10	0.30	0.70

and the Tikhonov reconstruction results, which illustrate that the proposed method enables quantitative reconstruction with better noise suppression and shape recovery.

VI. DISCUSSION

The ill condition of the system matrix of the MPI system renders the direct inverse of the linear equation unstable, and several regularizations have been proposed to solve this problem. The commonly used regularization approach, the Tikhonov penalty, provides a fast solution but leads to an over-smoothing problem. NFL regularization provides clear edge information; however, the l_1-norm and l_1-based near-isotropic TV norm used in NFL are biased estimates. Our experimental findings demonstrate that the reconstruction results obtained using NFL regularization significantly underestimate the intensity.

We propose a novel, nonconvex regularization method that can compensate for the concentration underestimation caused by NFL regularization and can precisely recover the intensity of a reconstructed image. In the proposed hybrid regularization, the nonconvex MC penalty was used to suppress the intensity bias produced by the l_1 penalty, and the TV penalty was added to ensure that the concentration distribution in the results was uniform. To avoid complex nonconvex objective problems, we chose MC regularization, which can be solved quickly using the firm threshold when the convexity condition is satisfied. Faced with the hybrid regularization of nonconvex MC and the isotropic TV penalty, the ADMM algorithm was employed to solve the problem; this algorithm transformed the problem into several simple subproblems for iteration. LU decomposition and the Chambolle projection method were adopted for acceleration in the subproblem solving.

We verified the validity of our proposed regularization method using simulated data, Open-MPI data, and homemade MPI data. A stenosis phantom, a vessel phantom with plaque in the main vessel, and overlapping ellipses of different intensities were used in the simulation. Reconstruction experiments were conducted using three phantoms with an SNR of 30 dB. The effectiveness of the method was verified through qualitative and quantitative comparisons. The accuracy and stability of the intensity recovery method were verified using overlapping elliptical phantom signals at different noise levels. The phantoms in the Open-MPI dataset and the data measured by a homemade MPI scanner were utilized to verify the generality of the proposed regularization on real-world data.

Although the proposed method enables more accurate image reconstruction, it may also introduce larger errors at the edges (see the error maps in Fig. 4). This may be due to the greater sparsity of the MC regularization we used, which is similar to concentrating a large range of errors into some pixel points at the edges.

The two-step method was used in our approach to simplify the selection of multiple parameters for the objective function with hybrid constraints. The noise related parameter ε was selected first, while β was selected using the adaptive updating strategy [35]. In the update strategy shown in (27), the smaller the update threshold κ, the smaller the value of β. In our experiments, the data acquired under the same conditions used the same κ: κ was set to 10 for the simulation data, and κ was set to 80 for the Open-MPI data. This non-specific setting may lead to the selection of non-optimal parameters and adversely affect the reconstruction results, such as the larger error at the edge pixels in Fig. 4 and the reconstruction results of the proposed method in Fig. 6, where some background noise exists near P1. While the quality of the reconstruction results can be improved by fine tuning, this approach is incompatible with the intent of simplifying the selection of parameters. A more refined multiparameter selection method may optimize this contradiction.

The point P4 in Fig. 6, which has the lowest concentration, cannot be reconstructed by either the proposed method or the NFL method. The proposed method suppresses the weak signals from low-concentration points while providing sufficient noise suppression, reducing the dynamic range of the reconstruction method. Therefore, in practice, the appropriate regularization term and reconstruction method need to be selected according to the specific needs. Meanwhile, high-quality reconstruction optimization methods that incorporate existing high dynamic range reconstruction methods remain to be investigated [39].

In Table VI, a comparison of the reconstruction times shows that although the proposed method achieved high-quality reconstruction, the reconstruction speed is still slower than that of the NFL method, which is a limitation of the proposed method. We consider that the NFL method achieves faster reconstruction because it converts the 2D problem into a 1D problem when solving the objective function [13]. However, we consider the runtime of the proposed method to be acceptable in non-real-time reconstruction scenarios. In addition, the current work is applicable to 2D reconstruction. In future research, the proposed method can be extended

TABLE VI
COMPUTATION TIME FOR THE RECONSTRUCTION EXPERIMENTS (UNIT: S)

		Tikhonov	NFL	Proposed
Phantom experiment (Fig. 3)	stenosis	1.58	0.72	1.88
	vessel	1.56	0.71	1.89
	ellipses	1.56	0.74	1.94
Ellipses phantom experiment (Fig. 4)	25 dB	1.63	0.71	1.83
	20 dB	1.64	0.73	1.87
	15 dB	1.58	0.71	1.85
Open-MPI Shape phantom experiment (Fig. 5)		0.033	0.054	0.131
Open-MPI Resolution phantom experiment (Fig. 6)		0.039	0.071	0.132
Measured data experiment (Fig. 7)		0.013	0.047	0.064

to 3D conditions, which will mainly involve improving the Chambolle projection algorithm presented in (25). Hence, the proposed methodology still needs to be optimized.

Recently, deep learning-based methods have made progress in MPI imaging [40], [41], [42], [43], [44], [45], [46], [47]. Through the use of substantial volumes of training data, learning-based methods can obtain accurate data distributions and priori information to achieve high-quality signal denoising [44], [47], system matrix optimization [42], [45], and image reconstruction [41], [46]. The design of regularizations in physics-driven reconstruction can optimize the loss function via deep learning methods [48]. Therefore, in future work, the proposed nonconvex regularization can be applied to optimize the reconstruction results of deep learning methods. In addition, direct comparisons between deep learning methods and physics-driven methods have yet to be performed, including the quality of the reconstruction results, the computation time, and the generalizability and robustness of the algorithms.

VII. CONCLUSION

In this study, we propose a regularization method that contains a nonconvex MC function and uses the ADMM algorithm to solve the optimization problem. During the iterative solution process, a subproblem containing nonconvex functions can maintain convexity and can be solved quickly by employing a threshold function. Reconstruction experiments on the simulated data, Open-MPI dataset, and the data measured by the homemade MPI scanner show that the proposed method outperforms the traditional Tikhonov and NFL regularizations and can alleviate the intensity underestimation problem existing in NFL regularization. The results demonstrate that the developed approach can achieve superior image quality while maintaining the quantitative advantages of MPI.

ACKNOWLEDGMENT

REFERENCES

[1] B. Gleich and J. Weizenecker, "Tomographic imaging using the non-linear response of magnetic particles," *Nature*, vol. 435, no. 7046, pp. 1214–1217, Jun. 2005.

[2] M. P. Bui, T.-A. Le, and J. Yoon, "A magnetic particle imaging-based navigation platform for magnetic nanoparticles using interactive manipulation of a virtual field free point to ensure targeted drug delivery," *IEEE Trans. Ind. Electron.*, vol. 68, no. 12, pp. 12493–12503, Dec. 2021.

[3] M. Ahlborg et al., "First dedicated balloon catheter for magnetic particle imaging," *IEEE Trans. Med. Imag.*, vol. 41, no. 11, pp. 3301–3308, Nov. 2022.

[4] J. J. Gevaert, C. Fink, J. D. Dikeakos, G. A. Dekaban, and P. J. Foster, "Magnetic particle imaging is a sensitive in vivo imaging modality for the detection of dendritic cell migration," *Mol. Imag. Biol.*, vol. 24, no. 6, pp. 886–897, Dec. 2022.

[5] Z. Peng et al., "Sensitive and quantitative in vivo analysis of PD-L1 using magnetic particle imaging and imaging-guided immunotherapy," *Eur. J. Nucl. Med. Mol. Imag.*, vol. 50, no. 5, pp. 1291–1305, Apr. 2023.

[6] W. Tong et al., "Sensitive magnetic particle imaging of haemoglobin degradation for the detection and monitoring of intraplaque haemorrhage in atherosclerosis," *eBioMedicine*, vol. 90, Apr. 2023, Art. no. 104509.

[7] H. Hui et al., "In vivo measurement of cerebral SPIO concentration in nonhuman primate using magnetic particle imaging detector," *IEEE Magn. Lett.*, vol. 14, pp. 1–5, 2023.

[8] F. Mohn, T. Knopp, M. Boberg, F. Thieben, P. Szwargulski, and M. Graeser, "System matrix based reconstruction for pulsed sequences in magnetic particle imaging," *IEEE Trans. Med. Imag.*, vol. 41, no. 7, pp. 1862–1873, Jul. 2022.

[9] L. Yin et al., "Recent developments of the reconstruction in magnetic particle imaging," *Vis. Comput. for Ind., Biomed., Art*, vol. 5, no. 1, p. 24, Oct. 2022.

[10] T. Knopp et al., "Weighted iterative reconstruction for magnetic particle imaging," *Phys. Med. Biol.*, vol. 55, no. 6, pp. 1577–1589, Mar. 2010.

[11] F. Lieb and T. Knopp, "A wavelet-based sparse row-action method for image reconstruction in magnetic particle imaging," *Med. Phys.*, vol. 48, no. 7, pp. 3893–3903, Jul. 2021.

[12] X. Chen, X. Han, and X. Tang, "Magnetic particle imaging reconstruction based on the least absolute shrinkage and selection operator regularization," *J. Med. Imag. Health Informat.*, vol. 11, no. 3, pp. 703–711, Mar. 2021.

[13] M. Storath et al., "Edge preserving and noise reducing reconstruction for magnetic particle imaging," *IEEE Trans. Med. Imag.*, vol. 36, no. 1, pp. 74–85, Jan. 2017.

[14] X. Chen, Z. Jiang, X. Han, X. Wang, and X. Tang, "Research of magnetic particle imaging reconstruction based on the elastic net regularization," *Biomed. Signal Process. Control*, vol. 69, Aug. 2021, Art. no. 102823.

[15] Z. Hu, F. Nie, R. Wang, and X. Li, "Low rank regularization: A review," *Neural Netw.*, vol. 136, pp. 218–232, Apr. 2021.

[16] K. M. Tan, L. Wang, and W.-X. Zhou, "High-dimensional quantile regression: Convolution smoothing and concave regularization," *J. Roy. Stat. Soc. Ser. B, Stat. Methodology*, vol. 84, no. 1, pp. 205–233, Feb. 2022.

[17] F. Li, Y. Ru, and X.-G. Lv, "Patch-based weighted SCAD prior for Rician noise removal," *J. Sci. Comput.*, vol. 90, no. 1, Jan. 2022, Art. no. 26.

[18] S. Liu, J. Cao, H. Liu, X. Zhou, K. Zhang, and Z. Li, "MRI reconstruction via enhanced group sparsity and nonconvex regularization," *Neurocomputing*, vol. 272, pp. 108–121, Jan. 2018.

[19] Y. Han et al., "Low-rank tucker-2 model for multi-subject fMRI data decomposition with spatial sparsity constraint," *IEEE Trans. Med. Imag.*, vol. 41, no. 3, pp. 667–679, Mar. 2022.

[20] Y. Shi, J. Huang, Y. Jiao, and Q. Yang, "A semismooth Newton algorithm for high-dimensional nonconvex sparse learning," *IEEE Trans. Neural Netw. Learn. Syst.*, vol. 31, no. 8, pp. 2993–3006, Aug. 2020.

[21] S. Shao, L. Zhang, H. Liu, P. Wang, and Q. Chen, "Images of 3-D maneuvering motion targets for interferometric ISAR with 2-D joint sparse reconstruction," *IEEE Trans. Geosci. Remote Sens.*, vol. 59, no. 11, pp. 9397–9423, Nov. 2021.

[22] G. Korats, S. Le Cam, R. Ranta, and V. Louis-Dorr, "A space-time-frequency dictionary for sparse cortical source localization," *IEEE Trans. Biomed. Eng.*, vol. 63, no. 9, pp. 1966–1973, Sep. 2016.

[23] H. Zhang, J. Qian, B. Zhang, J. Yang, C. Gong, and Y. Wei, "Low-rank matrix recovery via modified schatten-p norm minimization with convergence guarantees," *IEEE Trans. Image Process.*, vol. 29, pp. 3132–3142, 2020.

[24] I. Selesnick, "Sparse regularization via convex analysis," *IEEE Trans. Signal Process.*, vol. 65, no. 17, pp. 4481–4494, Sep. 2017.

[25] S. Ilbey et al., "Comparison of system-matrix-based and projection-based reconstructions for field free line magnetic particle imaging," *Int. J. Magn. Part. Imag.*, vol. 3, no. 1, pp. 1–8, 2017.

[26] T. Kluth, B. Jin, and G. Li, "On the degree of ill-posedness of multi-dimensional magnetic particle imaging," *Inverse Problems*, vol. 34, no. 9, Sep. 2018, Art. no. 095006.

[27] T. Kluth and B. Jin, "Enhanced reconstruction in magnetic particle imaging by whitening and randomized SVD approximation," *Phys. Med. Biol.*, vol. 64, no. 12, Jun. 2019, Art. no. 125026.

[28] T. Knopp et al., "Model-based reconstruction for magnetic particle imaging," *IEEE Trans. Med. Imag.*, vol. 29, no. 1, pp. 12–18, Jan. 2010.

[29] J. Weizenecker, B. Gleich, J. Rahmer, H. Dahnke, and J. Borgert, "Three-dimensional real-time in vivo magnetic particle imaging," *Phys. Med. Biol.*, vol. 54, no. 5, pp. L1–L10, Mar. 2009.

[30] M. Boberg, T. Knopp, P. Szwargulski, and M. Möddel, "Generalized MPI multi-patch reconstruction using clusters of similar system matrices," *IEEE Trans. Med. Imag.*, vol. 39, no. 5, pp. 1347–1358, May 2020.

[31] M. V. Afonso, J. M. Bioucas-Dias, and M. A. T. Figueiredo, "An augmented Lagrangian approach to the constrained optimization formulation of imaging inverse problems," *IEEE Trans. Image Process.*, vol. 20, no. 3, pp. 681–695, Mar. 2011.

[32] M. V. Afonso, J. M. Bioucas-Dias, and M. A. T. Figueiredo, "Fast image recovery using variable splitting and constrained optimization," *IEEE Trans. Image Process.*, vol. 19, pp. 2345–2356, 2010.

[33] H. E. Güven, A. Güngör, and M. Çetin, "An augmented Lagrangian method for complex-valued compressed SAR imaging," *IEEE Trans. Comput. Imag.*, vol. 2, no. 3, pp. 235–250, Sep. 2016.

[34] A. Chambolle, "Total variation minimization and a class of binary MRF models," in *Proc. Int. Workshop Energy Minimization Methods Comput. Vis. Pattern Recognit.*, 2005, pp. 136–152.

[35] S. Zhang, Y. Liu, X. Li, and D. Hu, "Enhancing ISAR image efficiently via convolutional reweighted l1 minimization," *IEEE Trans. Image Process.*, vol. 30, pp. 4291–4304, 2021.

[36] T. Knopp, P. Szwargulski, F. Griese, and M. Gräser, "OpenMPIData: An initiative for freely accessible magnetic particle imaging data," *Data Brief*, vol. 28, Feb. 2020, Art. no. 104971.

[37] L. Yin et al., "A streamlined 3-D magnetic particle imaging system with a two-stage excitation feed-through compensation strategy," *IEEE Trans. Instrum. Meas.*, vol. 72, pp. 1–10, 2023.

[38] K. Gräfe, A. von Gladiss, G. Bringout, M. Ahlborg, and T. M. Buzug, "2D images recorded with a single-sided magnetic particle imaging scanner," *IEEE Trans. Med. Imag.*, vol. 35, no. 4, pp. 1056–1065, Apr. 2016.

[39] M. Boberg, N. Gdaniec, P. Szwargulski, F. Werner, M. Möddel, and T. Knopp, "Simultaneous imaging of widely differing particle concentrations in MPI: Problem statement and algorithmic proposal for improvement," *Phys. Med. Biol.*, vol. 66, no. 9, May 2021, Art. no. 095004.

[40] P. Koch, M. Maass, M. Bruhns, C. Droigk, T. J. Parbs, and A. Mertins, "Neural network for reconstruction of MPI images," in *Proc. IWMPI*, 2019, pp. 39–40.

[41] B. Askin, A. Gungor, D. A. Soydan, E. U. Saritas, C. B. Top, and T. Cukur, "PP-MPI: A deep plug-and-play prior for magnetic particle imaging reconstruction," in *Proc. MLMIR*, Singapore, 2022, pp. 105–114.

[42] A. Güngör, B. Askin, D. A. Soydan, E. U. Saritas, C. B. Top, and T. Çukur, "TranSMS: Transformers for super-resolution calibration in magnetic particle imaging," *IEEE Trans. Med. Imag.*, vol. 41, no. 12, pp. 3562–3574, Dec. 2022.

[43] Y. Shang et al., "Deep learning for improving the spatial resolution of magnetic particle imaging," *Phys. Med. Biol.*, vol. 67, no. 12, Jun. 2022, Art. no. 125012.

[44] H. Peng et al., "Multi-scale dual domain network for nonlinear magnetization signal filtering in magnetic particle imaging," *Biomed. Signal Process. Control*, vol. 85, Aug. 2023, Art. no. 104863.

[45] G. Shi et al., "Progressive pretraining network for 3D system matrix calibration in magnetic particle imaging," *IEEE Trans. Med. Imag.*, vol. 42, no. 12, pp. 3639–3650, Dec. 2023.

[46] A. Güngör, B. Askin, D. A. Soydan, C. B. Top, E. U. Saritas, and T. Çukur, "DEQ-MPI: A deep equilibrium reconstruction with learned consistency for magnetic particle imaging," *IEEE Trans. Med. Imag.*, vol. 43, no. 1, pp. 321–334, Jan. 2024.

[47] Z. Wei, Y. Liu, T. Zhu, X. Yang, J. Tian, and H. Hui, "BSS-TFNet: Attention-enhanced background signal suppression network for time-frequency spectrum in magnetic particle imaging," *IEEE Trans. Emerg. Topics Comput. Intell.*, vol. 8, no. 2, pp. 1322–1336, Apr. 2024.

[48] H. Peng, Y. Li, X. Yang, J. Tian, and H. Hui, "Self-supervised signal denoising for magnetic particle imaging," in *Proc. EMBC*, 2023, pp. 1–4.